



# Path-Integrated Stereo X-Ray Digital Image Correlation: Resolving the Violation of Conservation of Intensity

EMC Jones<sup>1</sup>

Received: 7 August 2023 / Accepted: 28 December 2023 / Published online: 16 February 2024  
© Society for Experimental Mechanics 2024

## Abstract

**Background** X-ray imaging addresses many challenges with visible light imaging in extreme environments, where optical diagnostics such as digital image correlation (DIC) and particle image velocimetry (PIV) suffer biases from index of refraction changes and/or cannot penetrate visibly occluded objects. However, conservation of intensity—the fundamental principle of optical image correlation algorithms—may be violated if ancillary components in the X-ray path besides the surface or fluid of interest move during the test.

**Objective** The test series treated in this work sought to characterize the safe use of fiber-epoxy composites in aerospace and aviation industries during fire accident scenarios. Stereo X-ray DIC was employed to measure test unit deformation in an extreme thermal environment involving a visibly occluded test unit, incident surface heating to temperatures above 600°C, and flames and soot from combusting epoxy decomposition gasses. The objective of the current work is to evaluate two solutions to resolve the violation of conservation of intensity that resulted from both the test unit and the thermal chamber deforming during the test.

**Methods** The first solution recovered conservation of intensity by pre-processing the path-integrated X-ray images to isolate the DIC pattern of the test unit from the thermal chamber components. These images were then correlated with standard, optical DIC software. The second solution, called Path-Integrated Digital Image Correlation (PI-DIC), modified the fundamental matching criterion of DIC to account for multiple, independently-moving components contributing to the final image intensity. The PI-DIC algorithm was extended from a 2D framework to a stereo framework and implemented in a custom DIC software.

**Results** Both solutions accurately measured the cylindrical shape of the undeformed test unit, recovering radii values of  $R = 76.20 \pm 0.12$  mm compared to the theoretical radius of  $R_{theor} = 76.20$  mm. During the test, the test unit bulged asymmetrically as decomposition gasses pressurized the interior and eventually burned in a localized jet. Both solutions measured the heterogeneous radius of this bulge, which reached a maximum of approximately  $R = 91$  mm, with a discrepancy of 2–3% between the two solutions.

**Conclusions** Two solutions that resolve the violation of conservation of intensity for path-integrated X-ray images were developed. Both were successfully employed in a stereo X-ray DIC configuration to measure deformation of an aluminum-skinned, fiber-epoxy composite test unit in a fire accident scenario.

**Keywords** Digital Image Correlation (DIC) · X-rays · Path-integrated images · Optical flow · Conservation of intensity · Fiber-epoxy composite

---

EMC Jones is a member of SEM.

---

✉ EMC Jones  
emjones@sandia.gov

<sup>1</sup> SEM Fellow, Diagnostics for Extreme Environments and Hypersonics, Sandia National Laboratories, Albuquerque, NM, USA

## Introduction

Optical, non-contact diagnostics such as Digital Image Correlation (DIC) [1] and Particle Image Velocimetry (PIV) [2] are advantageous over their physical probe counterparts for kinematic measurements, as they are non-intrusive to the system being studied and provide full-field data instead of only point data. While extremely powerful and increasingly

common for experimental mechanics, optical DIC can suffer when applied to complex test configurations from disturbances in the air between the surface of interest and the camera, like heat waves or shocks [3–15]. Moreover, optical DIC and PIV do not allow for internal measurements, where the surface or fluid of interest is not directly visible.

X-ray imaging for DIC and PIV addresses many of the challenges with visible light imaging as X-rays do not refract through density gradients in air and are able to penetrate visibly opaque objects. X-ray DIC has been successfully used for many applications, where a high contrast image intensity pattern was created as X-rays were attenuated through either a naturally heterogeneous test unit or through a random pattern of a dense material applied onto or inside of a test unit [16–27]. X-ray imaging has similarly been employed for PIV to track velocities of opaque fluids [28–31]. The X-ray images are treated identically to optical images and are correlated with standard DIC and PIV software.

However, X-rays are attenuated by all of the components between the X-ray source and detector, resulting in path-integrated images. In order to use optical DIC and PIV algorithms with X-ray images, only the patterned surface or fluid of interest may move during the test. Any movement from ancillary objects along the path violates the conservation of intensity—the fundamental principal of optical algorithms—and standard DIC and PIV algorithms may fail to correlate the X-ray images.

The restriction on ancillary motion can be realized in simplified experimental configurations, but becomes impractical in more complex tests. To address this limitation, a novel DIC algorithm was recently proposed—Path-Integrated DIC (PI-DIC)—wherein the fundamental matching criterion was modified to account for multiple, independently-moving components contributing to the final image intensity [27]. PI-DIC was first verified with synthetic images of two plates undergoing independent rigid translations, rigid rotations, and uniform strains, and then demonstrated on a simplified exemplar experiment where two plates were rigidly translated. A single set of path-integrated images resolved 2D planar displacements and strains from each plate, independently, with 0.02 px and 0.05 px errors for the noisy synthetic images and experimental images, respectively.

The present work applies PI-DIC to a complex thermo-mechanical test of an aluminum-skinned, fiber-epoxy composite test unit, representative of aviation and aerospace components [32, 33]. The test unit was subjected to radiant heating to mimic a fire accident scenario. The safe use of fiber-epoxy composites in aviation/aerospace must consider their response to fire, as epoxy can decompose (degrading the strength of the component) and combust (adding an additional fuel source). Experimental data of the test unit temperature, internal pressurization due to epoxy decomposition, and external deformation from X-ray DIC were collected to

validate a computational model of the epoxy decomposition [33]. Regarding the X-ray DIC measurements, shadows from the heater rods of the thermal chamber appeared inconsistently between the two stereo views and moved during testing. Both of these artifacts corrupted the DIC pattern of the test unit.

The objectives of the current work are three-fold: (1) to extend PI-DIC from 2D, planar measurements to a stereo configuration for 3D measurements of a curved surface; (2) to demonstrate the applicability of PI-DIC to a complex test; and (3) to compare PI-DIC results to an alternative solution that corrects images to recover conservation of intensity so they can be processed with optical DIC software. The methods and results presented herein will serve as a baseline for extending X-ray DIC to challenging situations where motion of the surface of interest cannot be physically isolated from ancillary motion of other components in the path of the X-rays. Moreover, these methods developed for X-ray DIC have potential to be adapted for X-ray PIV as well.

The rest of the article is structured as follows. First, an overview of the experimental methods is presented in “[Experimental Methods](#)”. Then, the issues concerning violation of conservation of intensity for the path-integrated X-ray images are illustrated in “[Violation of Conservation of Intensity for Path-Integrated X-Ray Images](#)”. Next, the image pre-processing solution is summarized in “[Solution 1: Image Pre-Processing to Recover Conservation of Intensity](#)”, the background of 2D PI-DIC is recapitulated in the context of the current test series in “[2D path-integrated DIC \(PI-DIC\)](#)”, and the framework for stereo PI-DIC is developed in “[Extension to stereo PI-DIC](#)”. Then, the radius of the test unit is quantified using both X-ray DIC approaches, first in the reference configuration in “[Undeformed Test Unit Shape](#)”

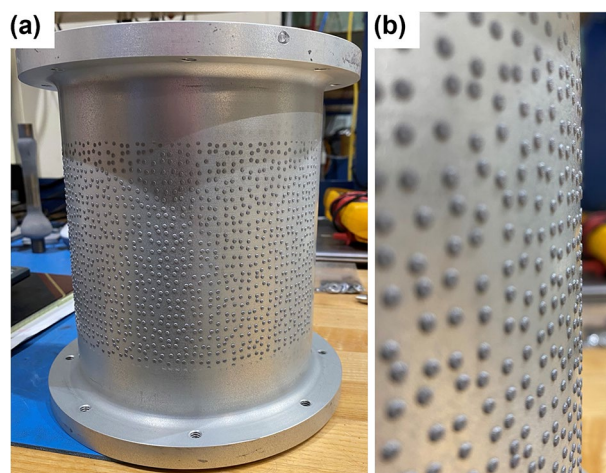
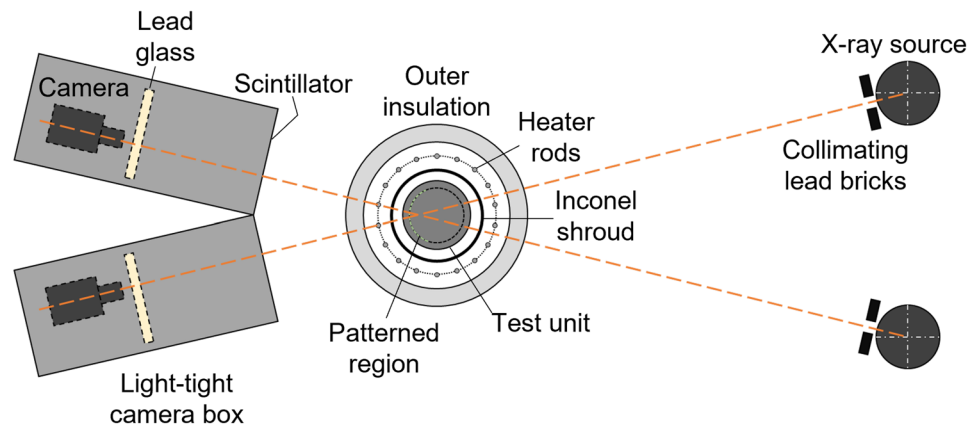


**Fig. 1** **a** Image of the aluminum-skinned, fiber-epoxy composite test unit (152.4 mm or 6 in. diameter) with **b** a magnified view of the tantalum DIC pattern

**Fig. 2** Top-down schematic of the experimental setup



and second in the deformed configuration as the test unit was heated and pressurized in “[Deformed Test Unit Shape](#)”. Finally, concluding remarks are made in “[Conclusions](#)”.

## Experimental Methods

Details of the experimental procedures for this test series are found in Ref. [32], while the salient points are briefly summarized here. The test unit, shown in Fig. 1, was comprised of a fiber-epoxy composite cylinder clad with a cylindrical aluminum skin, with an outer diameter of 152.4 mm (6 in.). Stainless steel end caps (not shown) were bolted to aluminum flanges on the top and bottom of the cylinder, creating a vessel that pressurized as the interior epoxy decomposed during the thermal test.

A high-contrast X-ray DIC pattern was generated with tantalum features, where the relatively dense tantalum more strongly attenuated X-rays and appeared dark in the images compared to the less dense aluminum and epoxy test unit that appeared as a light background. To create the pattern, a shadow mask was fabricated by milling holes at prescribed, pseudo-random locations in a flat sheet of stainless steel sheet metal, and then bending the sheet into a semi-circle to fit around the test unit. Tantalum powder was cold-sprayed through the shadow mask onto a region that was 190 mm (7.5 in.) circumferentially and 140 mm (5.5 in.) tall, corresponding to a 143° sector of the test unit. The resulting tantalum features were approximately 1.8 mm in diameter and 0.28 mm thick. The pattern feature density was purposefully sparser than the typical 50% target normally used for DIC [34] in order to keep the pattern and diagnostic minimally invasive to the system under study. A combined computational and experimental investigation verified that the tantalum dots had negligible influence on the thermo-mechanical properties of the test unit relative to other error sources [32].

The experimental setup is shown schematically in Fig. 2. The test unit was subjected to radiant heating in

a custom thermal chamber to mimic a fire environment. The chamber was comprised of a main ring of ceramic fiberboard insulation with two circular caps of insulation on the top and bottom. Eighteen resistive electrical heating rods were evenly distributed circumferentially. The rods heated an Inconel shroud, which in turn radiated uniformly to the test unit, leading to a temperature rise of the of the outer surface of the test unit of approximately 10 °C/min.

During testing, the gasses from the decomposing epoxy escaped the test unit and ignited, generating a continuous jet of flame, as shown in Fig. 3. Instrumentation such as strain gauges would not have survived this environment. The thermal chamber had no optical access for optical DIC, and modifying the thermal chamber to add a window would have altered the desired thermal boundary conditions. Even if there were optical access, the flames and soot from the decomposing gasses would have obfuscated optical cameras. Prior to ignition, visible light images

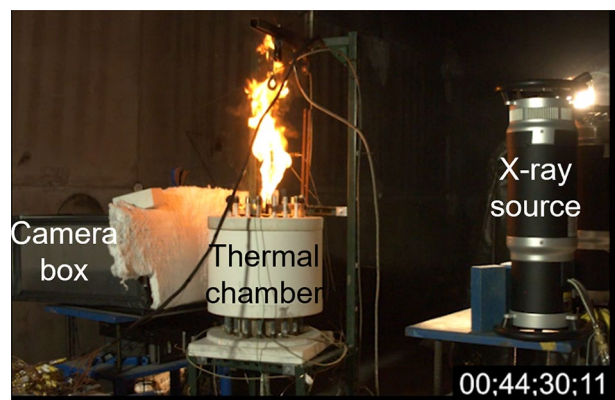


**Fig. 3** Overview image of the thermal chamber at 44.5 min into the test, when the test unit external temperature was 460 °C and the shroud was 600 °C. The lack of optical access, high temperatures, and flames and soot from combusting epoxy decomposition gas all motivated the need for X-ray DIC measurements to characterize the test unit deformation

**Table 1** Intrinsic and extrinsic parameters of the X-ray stereoscopic imaging system, using a pinhole camera model with no image distortions. Parameters  $c_x$  and  $c_y$  are the horizontal and vertical locations of the center point of the detector,  $f_x$  and  $f_y$  are the focal lengths in the

horizontal and vertical directions,  $\alpha$ ,  $\beta$ , and  $\gamma$  are the angles describing the rotations of each camera with respect to the world coordinate system, and  $t_x$ ,  $t_y$ , and  $t_z$  are the translations of each camera with respect to the world coordinate system

Intrinsic Parameters	Cam0	Cam1
$c_x$ (px)	3.064478132e+02	1.566626088e+02
$c_y$ (px)	-1.252512285e+02	5.912229298e+02
$f_x$ (px)	4.017806733e+03	4.202672971e+03
$f_y$ (px)	4.017806733e+03	4.202672971e+03
Extrinsic Parameters	Cam0	Cam1
$\alpha$ (deg.)	1.748341371e+02	-1.748677121e+02
$\beta$ (deg.)	-1.465172736e+01	1.466329476e+01
$\gamma$ (deg.)	7.934637613e-01	5.318890157e-01
$t_x$ (mm)	2.839832342e+02	-3.051012394e+02
$t_y$ (mm)	1.142600258e+01	-1.425242399e+01
$t_z$ (mm)	1.886425925e+02	2.466885104e+02

would have suffered severe distortions from heat waves. All of these factors motivated the use of X-ray DIC.

Two X-ray sources (Comet, Model: PXS EVO 300DSW) were arranged at a stereo angle of approximately  $28^\circ$ . Two scintillators (MCI Optonix, DRZ High) were placed on the opposite side of the thermal chamber, to convert X-rays to visible light. Two optical cameras (Andor NEO sCMOS) with lenses (Rokinon, ED AS IF UMC, 24 mm, f/1.4) imaged the back side of the scintillators, with an approximate field-of-view of  $180 \times 152 \text{ mm}^2$ . The optical cameras and lenses were placed in light-tight camera boxes to shield them from ambient light. Lead glass was placed in front of the cameras to reduce the number of X-rays that directly impinged upon the camera detectors.

The stereo X-ray imaging system was approximated by a distortion-free, pinhole camera model and was calibrated with a hybrid approach employing specialized dot-grid and speckled plate targets designed for X-ray imaging [24, 25, 32]. The final calibration parameters determined from Correlated Solutions Vic3D-9 are reported in Table 1.

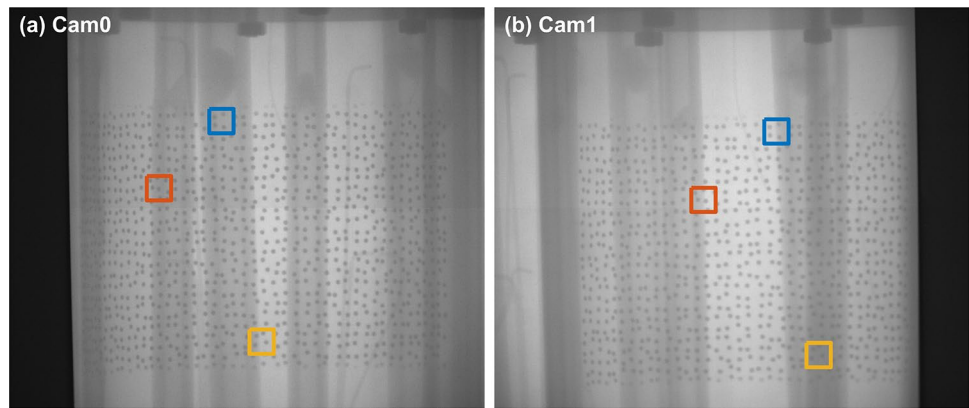
After images were captured *in situ*, a 4-frame temporal average was performed to reduce camera noise, leading to an effective frame rate of 0.5 Hz. Then, a 4-pixel outlier filter was applied to remove saturated pixels where X-rays directly impinged the camera detectors. Images were binned by a factor of 5 to further reduce noise and obtain DIC feature diameters closer to the optimal value of 3–5 px [34]. The final images had an effective size of  $512 \times 432 \text{ px}^2$ , effective image scale of 2.84 px/mm, and tantalum feature diameters of approximately 5.1 px.

## X-Ray DIC Analysis Methods

### Violation of Conservation of Intensity for Path-Integrated X-Ray Images

In the current test configuration, shadows from the heater rods appeared inconsistently in the path-integrated X-ray images. When correlation was attempted using standard, optical DIC software, it completely failed and returned zero valid data points. Increasing the subset size and adding additional, manually defined initializations were inadequate adjustments; correlation still failed and no data was generated. Only when the correlation thresholds were greatly relaxed to unreasonably large values were a few data points found; however, these data points were sporadic within the region-of-interest, the epipolar or projection error was unacceptably large (1–5 px), and the resulting shape measurement of the undeformed test piece was wildly inaccurate. In essence, the heater rod shadows violated conservation of intensity of the patterned surface of the test unit and completely prevented the use of optical DIC software for image analysis. These issues are illustrated in “[Static images of a stereo X-ray system](#)”, “[Temporal images of a 2D X-ray system](#)” and “[Pseudo light-field correction](#)”, and two solution approaches are presented in “[Solution 1: Image Pre-Processing to Recover Conservation of Intensity](#)” and “[Solution 2: Specialized Algorithm for Path-Integrated X-Ray Images](#)”.

**Fig. 4** Representative stereo pair of images from the two X-ray systems in the reference (undeformed) configuration. Three representative subsets are shown, emphasizing the different locations of the heater rod shadows relative to the DIC pattern in each image



**Static images of a stereo X-ray system**

The first issue was related to the correlation of images from one imaging system to the other in the stereo configuration. The heater rod shadows appeared in different locations in the two stereo images (Cam0 and Cam1) relative to the DIC pattern, emphasized by three representative subsets shown in Fig. 4.

The top subset (blue) appeared in the middle of a heater rod shadow in Cam0, giving the subset an overall darker background intensity; however, the same subset was partially over a different heater rod shadow in Cam1, leading to a sharp transition in background intensity within the subset. The middle subset (red) appeared on the edges of two different heater rods in each camera; the image intensity was lighter on the left side of the subset in Cam0 but on the right side in Cam1. The bottom subset (yellow) was located where two heater rod shadows overlapped in Cam1, giving the subset a particularly dark background, while the subset was on the edge of a heater rod shadow in Cam0. These discrepancies in image intensity caused stereo optical DIC software to fail to correlate the DIC pattern from Cam0 to Cam1, even for static images with no motion of either the heater rods or the test unit.

**Temporal images of a 2D X-ray system**

The second issue was related to correlation of images from one system over time. As the test unit deformed and the rods remained nominally stationary, the relative location of the heater rod shadows with respect to the DIC pattern changed over time, emphasized by a representative subset in Fig. 5.

The subset was initially centered horizontally on a heater rod shadow in the reference configuration (Fig. 5(a)). As the test unit deformed, the DIC pattern translated to the left. However, the rod remained nominally stationary, causing the subset of the DIC pattern to lay on the edge of the heater rod shadow in the deformed configuration (Fig. 5(b)). This motion of the deforming DIC pattern “over” a nominally stationary heater rod shadow caused 2D optical DIC to fail to correlate a single image series over time.

**Pseudo light-field correction**

In an attempt to address the issues with the heater rod shadows described in “Static images of a stereo X-ray system” and “Temporal images of a 2D X-ray system”, a pseudo light-field image was captured during the test setup, with the thermal chamber in place but without the test unit

**Fig. 5** Representative images at two points in time from the Cam0 X-ray system. A representative subset is shown, emphasizing the different locations of the heater rod shadows relative to the DIC pattern in each image

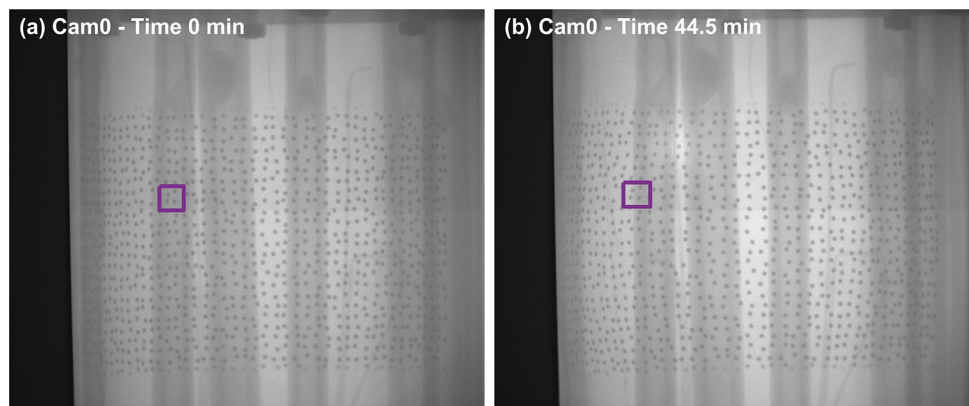


**Fig. 6** Pseudo light-field correction of test images: (a) Pseudo light-field image captured with the thermal chamber in place but no test unit. (b) Initial X-ray image of the test unit inserted into the thermal chamber, before pseudo light-field correction. (c)–(d) X-ray images after pseudo light-field correction at (c) the beginning of test and (d) 44.5 min into the test. Artifacts remaining after the correction are emphasized by the arrows

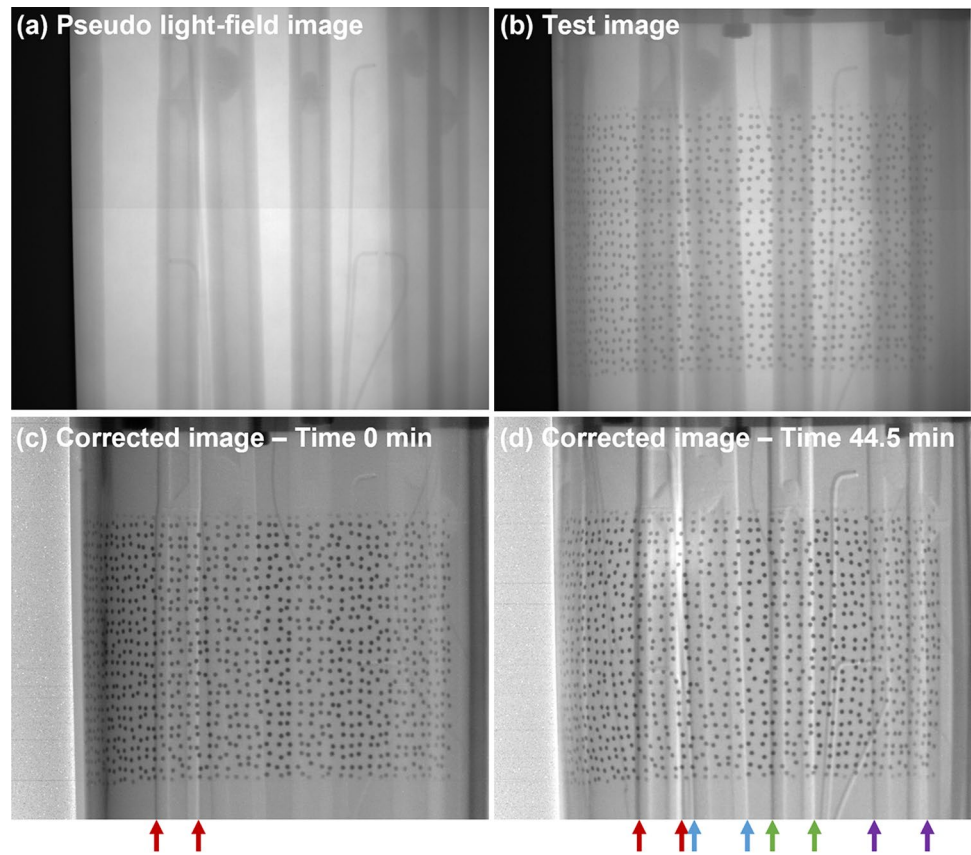


(Fig. 6(a)). Then, the test unit was carefully lowered into the thermal chamber and imaged (Fig. 6(b)). Finally, the test images captured *in situ* were divided by the pseudo light-field image to produce corrected test images that isolated the DIC pattern on the test unit from the thermal chamber (Fig. 6(c)–(d)).

Several of the heater rod shadows were effectively removed from the corrected image at the beginning of the test (Fig. 6(c)). However, some artifacts remained where a rod moved slightly during insertion of the test unit into the chamber, as indicated by the red arrows at the left and right edges of a heater rod. Additionally, during the test, all of the rods and thermocouple wires moved, and thus the artifacts increased over time (Fig. 6(d)). Because the rods did not remain perfectly stationary (both while the test unit was inserted into the chamber and during the test itself), the pseudo light-field correction was inadequate. Conservation of intensity of the corrected images (Fig. 6(c)–(d)) was still violated, and optical DIC software again failed to correlate these images.

### Solution 1: Image Pre-Processing to Recover Conservation of Intensity

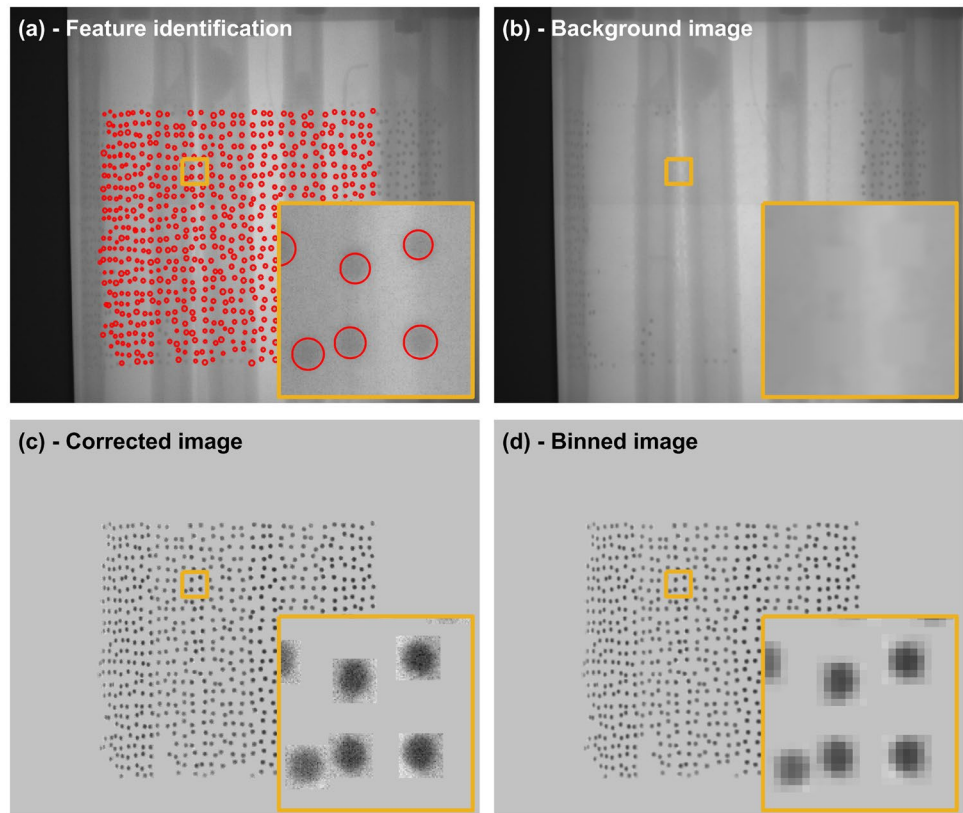
To overcome the challenges associated with conservation of intensity described in “[Violation of Conservation of](#)

[Intensity for Path-Integrated X-Ray Images](#)”, an image pre-processing routine was developed. The goal was to create a unique background image of the thermal chamber at every time step, to account for the moving heater rods.

The pre-processing steps are illustrated in Fig. 7. Starting with a full-resolution test image (before binning), the function `imfindcircles` was used in MATLAB to identify each of the individual tantalum features (Fig. 7(a)). Next, the pixels within a square region surrounding each feature were in-painted by interpolating from neighboring pixels, creating a background image (Fig. 7(b)). The original image was then divided by the background image to isolate the tantalum features (Fig. 7(c)). Finally, the full-resolution, corrected image was binned by a factor of 5 to reduce artifacts around the tantalum features, reduce image noise, and obtain feature diameters closer to the optimal value of 3–5 px as mentioned in “[Experimental Methods](#)”.

The image pre-processing steps were applied to each image in the time series, for each imaging system of the stereo configuration. The final corrected and binned images (e.g. Fig. 7(d)) were correlated using the user-defined settings shown in Table 2. Three optimization thresholds were used to discard poorly-correlated points: a consistency threshold, which evaluates the location of a point relative to its neighbors; a confidence margin, which evaluates the covariance matrix of the matching criterion;

**Fig. 7** Illustration of image pre-processing steps used to generate the final images correlated with standard (optical) DIC software. Magnified views depict a representative subset of  $135 \times 135 \text{ px}^2$  in the full-resolution images in (a)–(c) and  $27 \times 27 \text{ px}^2$  in the binned image in (d)



and a matchability threshold, which removes subsets with low contrast.<sup>1</sup>

The process outlined here was largely effective and allowed the use of commercial DIC software, designed for optical images, to process the corrected X-ray images. However, this solution suffered from two limitations. First, the feature identification algorithm was not wholly robust—some features were not identified, spurious features were sometimes erroneously identified, and artifacts remained around each feature in the corrected image (see magnified inset in Fig. 7(c)). Second, this approach is only viable for patterns consisting of easily identifiable features, such as the distinct, circular tantalum dots used here. Other types of patterns may not be as easily isolated, preventing the generalization of this approach.

**Solution 2: Specialized Algorithm for Path-Integrated X-Ray Images**

The limitations of Solution 1 described in “[Solution 1: Image Pre-Processing to Recover Conservation of Intensity](#)” inspired the development of a novel DIC algorithm

specifically for path-integrated X-ray images, called path-integrated DIC (PI-DIC). Rather than attempt to enforce or approximate conservation of intensity in order to use standard, optical DIC software, PI-DIC modifies the matching criterion—the core of the DIC algorithm—to account for multiple components moving independently in the path of the X-rays. The theoretical background for 2D PI-DIC, along with a demonstration using both synthetic and experimental images, is provided in Ref. [27]. In “[2D path-integrated DIC](#)

**Table 2** User-defined settings for DIC analysis using Solution 1 to pre-process the images to recover conservation of intensity

Parameter	Value
Software	Correlated Solutions, Vic3D-9
Subset size	27 px
Step size	3 px
Image pre-filtering	Default (3 × 3 binomial filter)
Intensity interpolant	Optimized 8-tap
Matching Criterion	Zero-normalized sum-of-squared differences (ZNSSD)
Subset shape function	Affine
Consistency threshold	0.02 px
Confidence margin	0.05 px
Matchability threshold	0.10 px

<sup>1</sup> See Correlated Solution’s documentation for details of these optimization thresholds at <https://downloads.correlatedsolutions.com/Vic-3D-9.4-Manual.pdf>, accessed 6 Apr 2023.

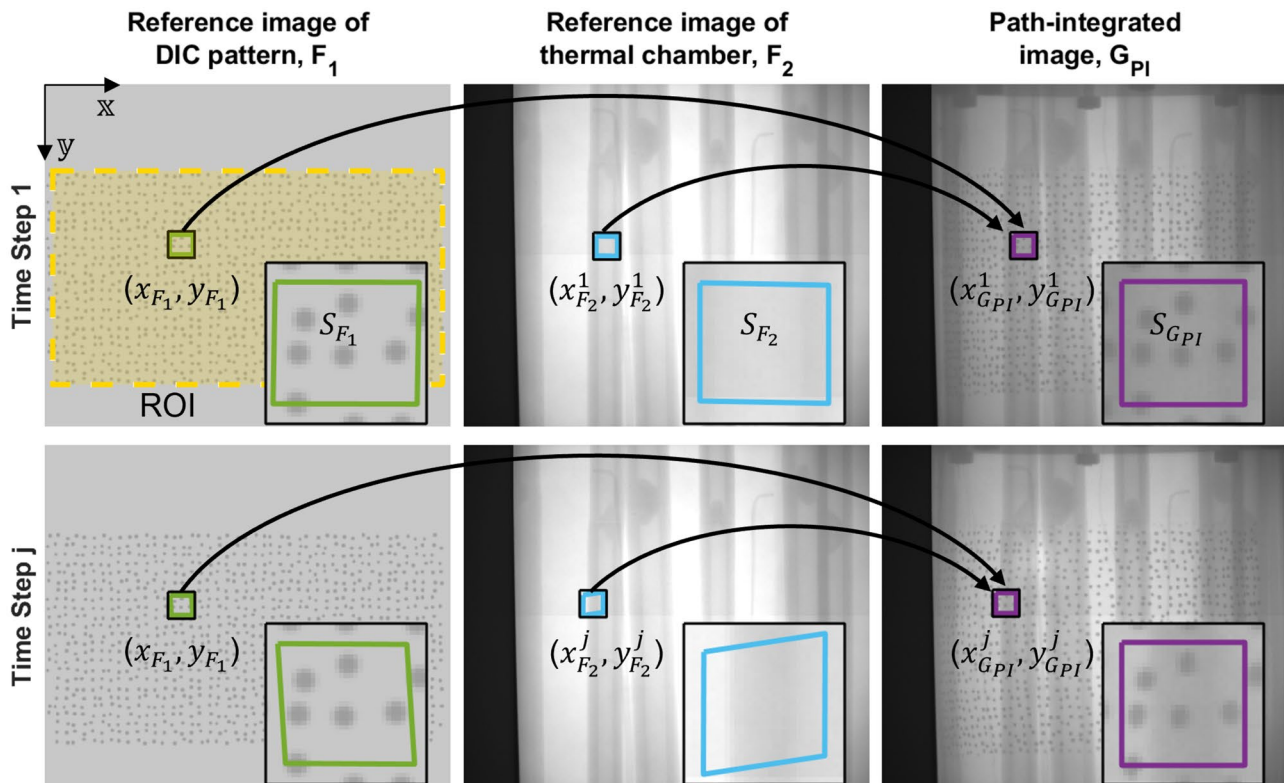


**Fig. 8** Schematic illustrating the correlation process for 2D PI-DIC. Left: Image  $F_1$  is a synthetic reference image for the DIC pattern. Middle: Image  $F_2$  is a pseudo light-field image of the thermal chamber without the test unit installed, captured experimentally prior to the test. Right: Image  $G_{pI}$  is a path-integrated image of the test unit in the thermal chamber captured experimentally *in situ* during the test. Two time steps are shown, of the undeformed configuration in the beginning of the test (time step 1, top row) and a representative image of the deformed configuration at 44.5 min (time step  $j$ , bottom row). A representative subset is shown across all three images and two time steps in the magnified insets

(PI-DIC)”, the key concepts for 2D PI-DIC are recapitulated in the context of the present thermo-mechanical test. In “[Extension to stereo PI-DIC](#)”, the extension to stereo PI-DIC is presented for the first time.

## 2D path-integrated DIC (PI-DIC)

**Reference images** In the current work, the components of the path-integrated X-ray images were separated into two groups—the patterned surface of the test unit and the heater rods of the thermal chamber. PI-DIC requires a reference image for each of these independent components, which may be acquired experimentally or generated synthetically, with different advantages for either option. Experimental reference images account for defects in the as-manufactured pattern compared to the as-designed pattern, but may not be possible to acquire (e.g. if the two groups of components cannot be physically isolated and imaged independently). Synthetic images are noise-free and can be generated from the as-designed pattern in cases where acquiring independent experimental images is not possible; however, synthetic images do not account for defects in the as-manufactured

pattern, which can lead to increased errors in the PI-DIC results [35].

In the present work, the first reference image of the DIC pattern on the test unit was generated synthetically based on the prescribed hole locations in the shadow mask in the flat configuration, before the mask was bent around the test unit (see “[Experimental Methods](#)”). This image, denoted as  $F_1$ , is shown in Fig. 8. Generating the reference image in the flat configuration facilitated correlation between the two imaging systems for stereo PI-DIC, as described in “[Extension to stereo PI-DIC](#)”.

The background intensity and feature intensity of image  $F_1$  were prescribed to be 1330 and 1050 counts on a 16-bit scale, respectively, based on estimations from the full-resolution experimental images. A super-resolution image was created first ( $25600 \times 21600 \text{ px}^2$ ) with feature diameters of 229 px, then binned by a factor of 10 to match the full-resolution size of the experimental images ( $2560 \times 2160 \text{ px}^2$ ). Next, the image was smoothed with a Gaussian filter (`imgaussfilt` function in MATLAB, standard deviation of 3 px) to approximate the blur inherent in the experimental



images. Finally, the image was binned further by a factor of 5 to match the size of the binned experimental images ( $512 \times 432$  px<sup>2</sup>).

The second reference image was taken to be the experimentally-captured pseudo light-field image acquired with the thermal chamber in place but with no test unit installed. This image, denoted as  $F_2$ , is also shown in Fig. 8. As with the test images themselves, this pseudo light-field image was also binned by a factor of 5 to a final image size of  $512 \times 432$  px<sup>2</sup>.

**Subset shape function parameters** PI-DIC was formulated using a local or subset-based approach, wherein the region-of-interest (ROI, yellow dashed rectangle in Fig. 8) was divided into a grid of localized regions or subsets. Fig. 8 and the following discussion illustrate the subset shape function parameters for a representative subset. Full field data was obtained by analyzing all subsets in the ROI.

Consider a representative subset in the reference image of the DIC pattern,  $S_{F_1}$ . The coordinates of the center point of the subset— $(x_{F_1}, y_{F_1})$  in the image coordinate system defined by axes  $x$  and  $y$ —are prescribed by the user and remain constant over time. Even though there is only a single reference image  $F_1$  (i.e.  $F_1$  remains constant over time), the subset  $S_{F_1}$  is allowed to deform over time as the test unit deforms. Four warping parameters from an affine shape function describe the subset deformation— $P_{xx,F_1}^j, P_{xy,F_1}^j, P_{yx,F_1}^j$ , and  $P_{yy,F_1}^j$ , where the superscript  $j$  represents the index in the time series of images. This warping is highlighted by the green quadrilateral subset shapes in the magnified insets in Fig. 8 at both time step 1 (top row) and time step  $j$  (bottom row).

For a given subset in the first reference image,  $S_{F_1}$ , a corresponding subset exists in the path-integrated image,  $S_{G_{PI}}$ , indicated by the purple squares in Fig. 8. This subset must remain square, but the center of it can translate according to two translation parameters from an affine shape function,  $P_{u,G_{PI}}^j = x_{G_{PI}}^j - x_{F_1}$  and  $P_{v,G_{PI}}^j = y_{G_{PI}}^j - y_{F_1}$ , where  $(x_{G_{PI}}^j, y_{G_{PI}}^j)$  are the coordinates of the subset center at time step  $j$  in the series of images.

Finally, the intensity of subset in the path-integrated image,  $S_{G_{PI}}$ , is a function of X-ray attenuation through both the test unit and the thermal chamber. Therefore, the corresponding subset in the thermal chamber image,  $S_{F_2}$ , must also be identified, indicated by the blue quadrilaterals in Fig. 8. Similar to  $F_1$ , there is also only a single reference image  $F_2$  (i.e.  $F_2$  is also constant over time). However, the subset  $S_{F_2}$  can both translate according to the two translation parameters,  $P_{u,F_2}^j = x_{F_2}^j - x_{F_1}$  and  $P_{v,F_2}^j = y_{F_2}^j - y_{F_1}$ , as well as warp according to the four warping parameters,  $P_{xx,F_2}^j, P_{xy,F_2}^j, P_{yx,F_2}^j$ , and  $P_{yy,F_2}^j$ .

In sum, 12 affine shape function parameters describe the independent motion and deformation of the test unit and the thermal chamber:

$$P_{PI} = [P_{xx,F_1}, P_{xy,F_1}, P_{yx,F_1}, P_{yy,F_1}, P_{u,F_2}, P_{v,F_2}, P_{xx,F_2}, P_{xy,F_2}, P_{yx,F_2}, P_{yy,F_2}, P_{u,G_{PI}}, P_{v,G_{PI}}] \quad (1)$$

These parameters must be identified for each subset in the ROI at each time step. (For clarity, the superscripts  $j$  have been omitted in equation (1)).

In general, PI-DIC can be used to track motion/deformation of two (or more) independent patterns. In this test specifically, the intrinsic pattern of the thermal chamber components (image  $F_2$ ) lacked sufficient intensity gradients, especially in the vertical direction, to be well tracked on its own. As a result, subsets in image  $F_2$  were frequently poorly identified, with unrealistically large warping parameters (such as the large shear shown at time step  $j$  in Fig. 8) and large vertical displacements. However, the 6 identified subset shape function parameters associated with subsets in image  $F_2$  were sufficiently accurate to account for the intensity contribution of the thermal chamber in the path-integrated images  $G_{PI}$ . Thus, while all 3 images and all 12 shape function parameters were necessary to perform the correlation, only the two translation parameters associated with the path-integrated images,  $P_{u,G_{PI}}^j$  and  $P_{v,G_{PI}}^j$ , were ultimately used to describe the deformation of the test unit, as discussed in “Extension to stereo PI-DIC”.

**Matching criterion** After the subset shape function parameters are applied to subsets in the two individual reference images, a single reference subset is composed using an approximation of the Beer-Lambert Law:

$$S_{F_{PI}} = \frac{1}{F_0} S_{F_1} S_{F_2} \quad (2)$$

where  $F_0$  is the unimpeded X-ray image intensity.

Conservation of intensity is then formulated similar to optical DIC, where the composed reference subset,  $S_{F_{PI}}$ , is approximately equal to the experimental, path-integrated subset,  $S_{G_{PI}}$ . Since equality between the two subsets cannot be practically realized, a zero-normalized, sum-of-squared differences (ZNSSD) matching criterion [36],  $\Psi$ , is employed to express the difference between the two subsets:

$$\Psi = \sqrt{\sum_{k \in \Omega} \left( \frac{\bar{F}_k}{\sqrt{\sum \bar{F}_k^2}} - \frac{\bar{G}_k}{\sqrt{\sum \bar{G}_k^2}} \right)^2} \quad (3)$$

with

**Table 3** User-defined settings for DIC analysis using Solution 2 with a specialized path-integrated DIC algorithm

Parameter	Value
Software	Customized PI-DIC algorithm implemented in MATLAB
Subset size	27 px
Step size	3 px
Image pre-filtering	imgaussfilt, standard deviation of 0.5 px, filter size of 3 px
Intensity interpolant	Cubic spline
Matching Criterion	Zero-normalized sum-of-squared differences (ZNSSD)
Subset shape function	Affine (customized for PI-DIC)
Optimizer	Gradient-based, nonlinear, constrained optimizer <code>fmincon</code> <sup>a</sup> : Forward finite-difference Optimality tolerance of $1 \cdot 10^{-8}$ Step tolerance of $1 \cdot 10^{-8}$ Function evaluation limit of 5000 Iteration limit of 500
Matching criterion threshold	$\Psi_{thresh} = 0.4$ px (equation (3))
Back-projection threshold	$\delta_{thresh} = 0.2$ px (equation (14))

<sup>a</sup>See MATLAB's documentation for details of the optimizer options at <https://www.mathworks.com/help/optim/ug/fmincon.html> and <https://www.mathworks.com/help/optim/ug/optimization-options-reference.html>, accessed 19 December 2022

$$\bar{F}_k = F_k - \bar{F} \quad (4a)$$

$$\bar{G}_k = G_k - \bar{G} \quad (4b)$$

and

$$\bar{F} = \frac{1}{K} \sum_{k \in \Omega} F_k \quad (5a)$$

$$\bar{G} = \frac{1}{K} \sum_{k \in \Omega} G_k \quad (5b)$$

where  $F_k$  and  $G_k$  are intensity values at the  $k$ 'th pixel of the composed, path-integrated reference subset,  $S_{F_{PI}}$ , or the experimental, path-integrated subset,  $S_{G_{PI}}$ , respectively, and the sum is carried out over the  $K$  pixels contained in the subset  $\Omega$ .

With the ZNSSD criterion, the scaling effect of the  $\frac{1}{F_0}$  multiplier in equation (2) in the main text is removed, and thus the unimpeded X-ray image intensity,  $F_0$ , does not need to be measured experimentally. Additionally, the ZNSSD criterion partially mitigates uncertainties in the intensity values used to generate the synthetic reference image of the DIC pattern,  $F_1$ .

The matching criterion was computed for every subset in the ROI and for every image in the time series. Any subsets with a matching criterion residual exceeding the manually-defined threshold of  $\Psi_{thresh} = 0.4$  px were removed from further analysis.

**Optimization algorithm** An optimization algorithm is employed to identify the 12 parameters  $\mathbf{P}_{PI}^*$  that minimize the value of the matching criterion:

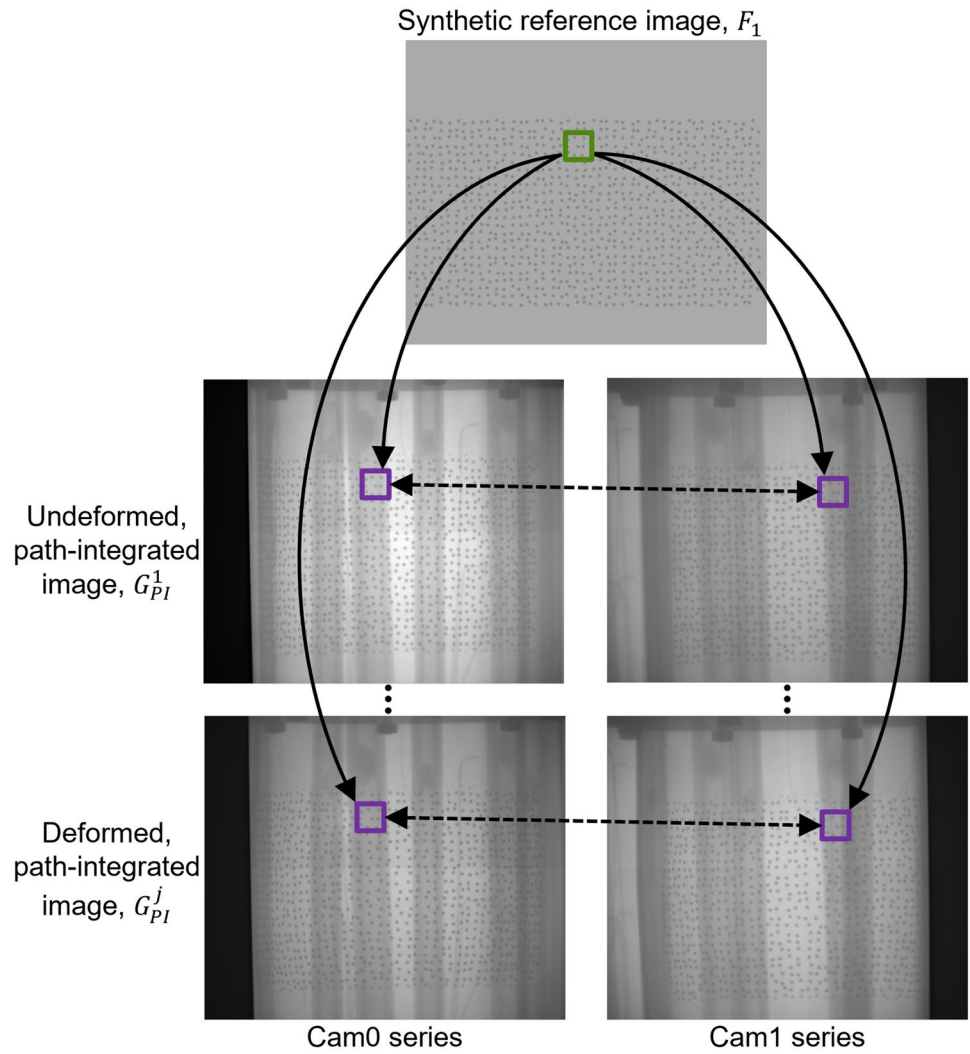
$$\mathbf{P}_{PI}^* = \arg \min_{\mathbf{P}_{PI}} (\Psi) \quad (6)$$

User-defined settings for the correlation are shown in Table 3. Details of the initialization of the optimization algorithm are given in the Appendix.

### Extension to stereo PI-DIC

**Matched points from Cam0 to Cam1** 2D PI-DIC is first performed for each X-ray imaging system (Cam0 and Cam1) individually. In this process, subsets are mapped from the synthetic reference image,  $F_1$ , to the undeformed, path-integrated image,  $G_{PI}^1$ , and through the series of deformed, path-integrated images,  $G_{PI}^j$  (where the superscript  $j$  represents the index in the time series of images), as illustrated by the solid arrows in Fig. 9. As a consequence, a mapping is also naturally created from Cam0 to Cam1 for each subset at each time step, illustrated by the dashed arrows. Note that by using a synthetic reference image in the “flat” configuration for  $F_1$ , no direct correlation is performed between the path-integrated image for Cam0 and the path-integrated image for Cam1, as is typically done for standard stereo-DIC.

**Fig. 9** Illustration of stereo PI-DIC. Each subset in the synthetic reference image,  $F_1$ , was correlated through the series of path-integrated images,  $G_{PI}^j$ , for Cam0 and Cam1 individually (solid arrows). Through these two sets of 2D correlations, subsets were also naturally matched between Cam0 and Cam1 at each time step (dashed arrows). For illustrative purposes, only a single subset is shown, but in actuality, these mappings were created for all subsets in the ROI



This mapping provides the centers of corresponding subsets in the Cam0 and Cam1 path-integrated images, namely  $\mathbf{x}_{m,Cam0}^j = (x_{G_{PI,Cam0}^j}^j, y_{G_{PI,Cam0}^j}^j)$  and  $\mathbf{x}_{m,Cam1}^j = (x_{G_{PI,Cam1}^j}^j, y_{G_{PI,Cam1}^j}^j)$ , where the subscript  $m$  stands for “matched” points. These matched points are the first required input for stereo-DIC.

**Camera projection matrices** The second input required for stereo-DIC is the projection matrices for both cameras,  $\lambda$ , which relate the camera image coordinates to the world coordinates. These matrices are calculated from the intrinsic and extrinsic camera calibration parameters obtained from the hybrid stereo calibration (Table 1) as follows.

First, the  $\mathbf{K}$  matrices are defined from the intrinsic parameters as:

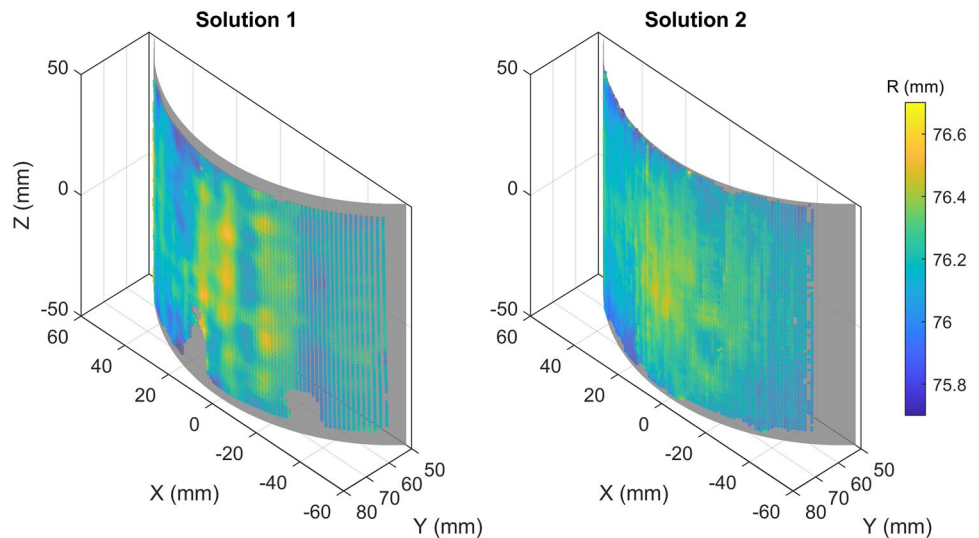
$$(\mathbf{K}_i)_{3 \times 4} = \begin{bmatrix} f_{x_i} & s_i & c_{x_i} & 0 \\ 0 & f_{y_i} & c_{y_i} & 0 \\ 0 & 0 & 1 & 0 \end{bmatrix} \quad (7)$$

where the subscript  $i$  represents either Cam0 or Cam1. Next, the rotation matrices,  $\mathbf{R}$ , are defined from the extrinsic orientation angles for each camera as:

$$\mathbf{D}_i = \begin{bmatrix} 1 & 0 & 0 \\ 0 & \cos(\alpha_i) & \sin(\alpha_i) \\ 0 & -\sin(\alpha_i) & \cos(\alpha_i) \end{bmatrix} \quad (8a)$$

$$\mathbf{C}_i = \begin{bmatrix} \cos(\beta_i) & 0 & -\sin(\beta_i) \\ 0 & 1 & 0 \\ \sin(\beta_i) & 0 & \cos(\beta_i) \end{bmatrix} \quad (8b)$$

**Fig. 10** 3D view of the undeformed test unit, as measured with stereo X-ray DIC using either Solution 1 to pre-process the images to recover conservation of intensity or Solution 2 using a specialized path-integrated DIC algorithm. The colormap represents the computed radius of the two point clouds. The gray cylinder represents the theoretical test unit shape with radius of  $R_{theor} = 76.2$  mm



$$\mathbf{B}_i = \begin{bmatrix} \cos(\gamma_i) & \sin(\gamma_i) & 0 \\ -\sin(\gamma_i) & \cos(\gamma_i) & 0 \\ 0 & 0 & 1 \end{bmatrix} \quad (8c)$$

$$(\mathbf{R}_i)_{3 \times 3} = (\mathbf{D}_i \mathbf{C}_i \mathbf{B}_i)^T \quad (8d)$$

The translation vectors,  $\mathbf{t}$ , are taken directly from the extrinsic translation parameters as:

$$(\mathbf{t}_i)_{3 \times 1} = [t_{x_i} \ t_{y_i} \ t_{z_i}]^T \quad (9)$$

Then, the rotation matrices and translation vectors are concatenated as:

$$(\mathbf{T}_i)_{4 \times 4} = \begin{bmatrix} \mathbf{R}_i & \mathbf{t}_i \\ \mathbf{0} & 1 \end{bmatrix} \quad (10)$$

Finally, the  $\lambda$  matrices are computed by multiplying the intrinsic matrices  $\mathbf{K}$  with the concatenated extrinsic matrices  $\mathbf{T}$ :

$$(\lambda_i)_{3 \times 4} = \mathbf{K}_i \mathbf{T}_i \quad (11)$$

**Triangulation to 3D world coordinates** Given a set of matched points between Cam0 and Cam1,  $\mathbf{x}_{m,i}^j$ , and the two camera projection matrices,  $\lambda_i$ , the function `triangulate` is used in MATLAB<sup>2</sup> to compute the 3D world coordinates of each subset at each time step,  $\mathbf{X}^j = [X, Y, Z]^T$ . These world coordinates describe the three-dimensional shape of the patterned surface of the cylindrical test unit as it deforms during the test.

<sup>2</sup> See MATLAB's documentation at <https://www.mathworks.com/help/vision/ref/triangulate.html>, accessed 11 May 2023.

**Back-projection** As an error metric, the 3D world coordinate point is back-projected to each of the image coordinates according to:

$$\begin{bmatrix} \mathbf{x}_{p,i}^j \\ 1 \end{bmatrix} = \frac{1}{\alpha_i^j} \lambda_i \begin{bmatrix} \mathbf{X}^j \\ 1 \end{bmatrix} \quad (12)$$

where  $\mathbf{x}_{p,i}^j$  are the locations of the back-projected points in image coordinates. The scalar  $\alpha$  is given by:

$$\alpha_i^j = \mathbf{R}_{i,3} \mathbf{X}^j + \mathbf{t}_{i,3} \quad (13)$$

where  $\mathbf{R}_{i,3}$  is the third row of the rotation matrix  $\mathbf{R}_i$ , and  $\mathbf{t}_{i,3}$  is the third entry in the translation vector  $\mathbf{t}_i$ . The back-projection error,  $\delta_i^j$ , is defined as the distance between the original matched point location,  $\mathbf{x}_{m,i}^j$ , and the back-projected point location,  $\mathbf{x}_{p,i}^j$ :

$$\delta_i^j = |\mathbf{x}_{m,i}^j - \mathbf{x}_{p,i}^j| \quad (14)$$

The back-projection error was calculated for every subset in the ROI, for both X-ray imaging systems (Cam0 or Cam1), and for every image in the time series. Any subsets with a back-projection value exceeding the manually-defined threshold of  $\delta_{thresh} = 0.2$  px was removed from further analysis.

## Results and Discussion

### Undeformed Test Unit Shape

After stereo X-ray DIC was performed using either Solution 1 or Solution 2, a cylindrical coordinate system was

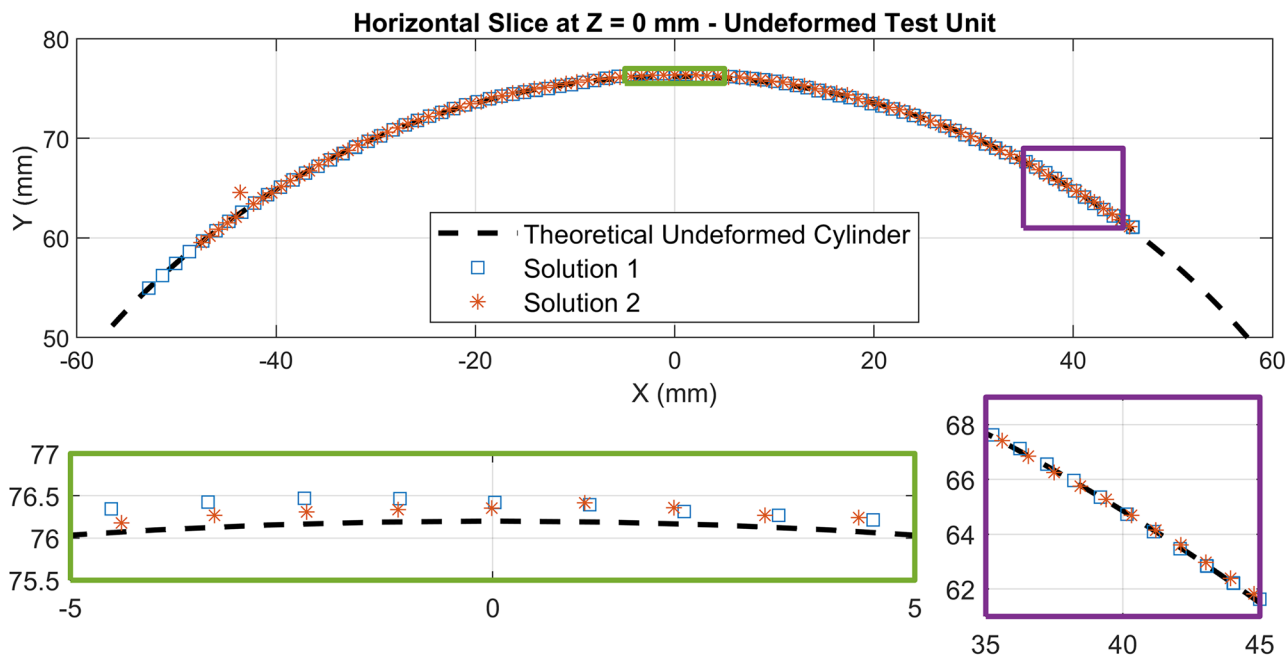


**Fig. 11** 2D slice in the  $X - Y$  plane at  $Z = 0$  mm of the undeformed test unit, as measured with stereo X-ray DIC using either Solution 1 to pre-process the images to recover conservation of intensity or Solution 2 using a specialized path-integrated DIC algorithm. The black dashed line represents the theoretical test unit shape with radius of  $R_{theor} = 76.2$  mm. Two magnified views are shown for the center (green box) and side (purple box) of the ROI

defined. The point cloud of the undeformed test unit was fit in a least-squares sense to a cylinder with the theoretical test unit radius of  $R_{theor} = 76.2$  mm. Then, alignment along the longitudinal axis was performed manually by setting  $Z = 0$  for a specific tantalum feature in the center of the ROI.

A three-dimensional view of the undeformed test unit shape is shown in Fig. 10 for both solutions, and a two-dimensional slice in the  $X - Y$  plane at  $Z = 0$  mm is shown in Fig. 11. Qualitatively, both DIC point clouds fit the theoretical cylinder well over the entire ROI. Solution 1 presents some vertical striations in the computed radius, while Solution 2 is somewhat more uniform. Both solutions show a slightly larger radius towards the center of the ROI, as highlighted by the first magnified inset (green box) in Fig. 11. This oversized radius could either be a true deviation of the as-manufactured part from the theoretical radius, or could be an artifact of the stereo calibration that is consistent for both data sets from the two solution methods. Towards the sides of the ROI, the computed radius agrees more closely with the theoretical radius, as highlighted by the second magnified inset (purple box) in Fig. 11.

Both solutions have some points that correlated poorly and are removed based on the thresholds described in “Solution 1: Image Pre-Processing to Recover Conservation of Intensity” (Table 2) and “Solution 2: Specialized Algorithm for Path-Integrated X-Ray Images” (Table 3), for Solution

1 and Solution 2, respectively. These omitted data points result in the blank areas in Fig. 10. Focusing on the center of the ROI between  $-40 \leq X \leq 40$  mm and  $-40 \leq Z \leq 40$  mm to avoid artifacts near the edges of the ROI, Solution 1 has 111 omitted points (out of 5225, or 2.1%) while Solution 2 has no omitted points (out of 5628).<sup>3</sup> Thus, for static images captured before the test began, Solution 2 is more robust compared to Solution 1.

To quantify these results, the radius was computed for all points in the ROI, for five static images. The mean and standard deviation of the computed radii are identical for both solutions, with values of  $R = 76.20 \pm 0.12$  mm. These values indicate excellent accuracy and precision of the two approaches of stereo X-ray DIC in this challenging environment.

<sup>3</sup> The initial grid of interrogation points was defined with a step size of 3 px, on either the experimental reference image for Cam0 for Solution 1, or in the synthetic “flat” reference image for Solution 2. Due to the curvature of the test unit, a constant step size of 3 px resulted in fewer data points for Solution 1 (5225) compared to Solution 2 (5628).



Fig. 12 Postmortem image of the test unit

## Deformed Test Unit Shape

### Overview

Figure 12 presents a post mortem image of the test unit, showing a bulge towards the tantalum pattern, with the opposite side remaining straight. It is hypothesized that additional heat flux

from a biased placement of the test unit in the thermal chamber and a localized combusting jet of decomposition gasses (see Fig. 3) caused the asymmetric deformation. The complete thermo-mechanical response of the test unit, combining temperature, interior pressure, and deformation measurements, is analyzed in Ref. [32]. The present work focuses on evaluating the efficacy of the stereo X-ray DIC diagnostic for obtaining deformation measurements and on comparing the two analysis solutions described in “X-Ray DIC Analysis Methods”.

Figure 13 shows a three-dimensional view of the deformed test unit shape near the end of the test, and Fig. 14 shows the corresponding slice through the  $X - Y$  plane at  $Z = 0$  mm. The bulge observed qualitatively post mortem in Fig. 12 is thus quantified through stereo X-ray DIC measurements, with a peak radius of approximately 91 mm, or a change in radius of approximately 15 mm.

### Poorly-correlated points

As mentioned in “Undeformed Test Unit Shape”, both solutions suffer from points that correlated poorly and were removed based on prescribed thresholds (Tables 2 and 3). Again focusing on the center of the ROI between  $-40 \leq X \leq 40$  mm and  $-40 \leq Z \leq 40$  mm, Solution 1 retains between 95–97% of points in the ROI, while Solution 2 retains more than 99% of points for the majority of the test.

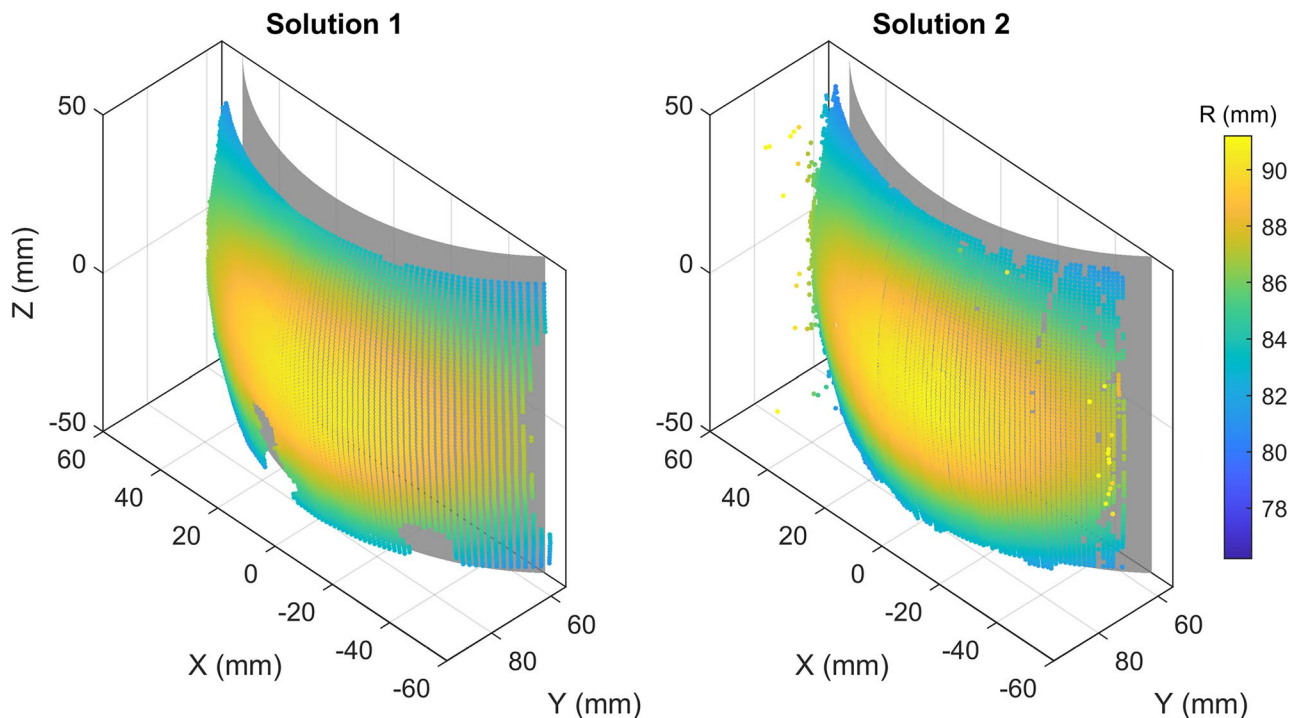
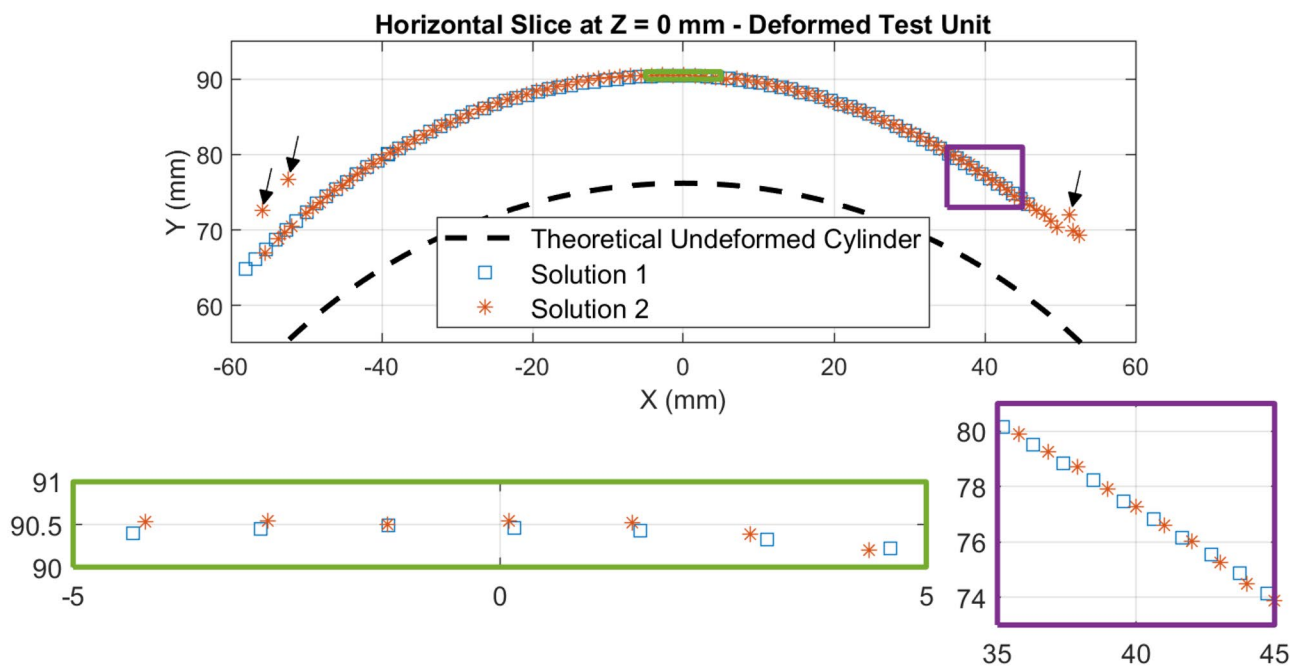


Fig. 13 3D view of the deformed test unit near the end of the test, as measured with stereo X-ray DIC using either Solution 1 to pre-process the images to recover conservation of intensity or Solution 2 using a specialized path-integrated DIC algorithm. The colormap represents the computed radius of the two point clouds. The gray cylinder represents the theoretical, undeformed test unit shape with radius of  $R_{theor} = 76.2$  mm



**Fig. 14** 2D slice in the  $X - Y$  plane at  $Z = 0$  mm of the deformed test unit near the end of the test, as measured with stereo X-ray DIC using either Solution 1 to pre-process the images to recover conservation of intensity or Solution 2 using a specialized path-integrated DIC algorithm. The black dashed line represents the theoretical, undeformed test unit shape with radius of  $R_{theor} = 76.2$  mm. Arrows indicate poorly-correlated points in Solution 2 that were not removed based on the manually-defined thresholds (Table 3). Two magnified views are shown for the center (green box) and side (purple box) of the ROI

For Solution 1, the poorly-correlated points occur in regions where the `imfindcircles` function failed to identify all the tantalum features (see Fig. 7). This missing data highlights one of the main limitations of Solution 1, namely, the feebleness of the feature identification algorithm. While the algorithm could be improved, Solution 1 is still limited to easily isolated pattern features, such as the circular dots used in the present work, preventing the generalization of this approach to other types of patterns.

For Solution 2, there are some points, typically near the outer edges of the ROI, that are obviously spurious but are not removed based on the prescribed thresholds; see, for instance, the points indicated by arrows in Fig. 14. Similar to determining appropriate initializations for DIC (see the Appendix), designing discriminating thresholds that retain well-correlated data points but discard poorly-correlated data points is non-trivial, even for optical DIC. Improving the thresholds in the PI-DIC code so that spurious points are not retained, and/or incorporating PI-DIC into an established DIC software that already has more advanced thresholds, is a subject for future work.

**Deformation over time**

Figure 15 presents a time trace of the radius for a single point at the center of the ROI at  $(X, Z) = (0, 0)$  mm. Unlike the

undeformed test unit shape, there is no known ground truth for the deformed shape. However, both solutions agree well overall and capture the interesting temporal evolution of the test unit deformation *in situ* during the test.

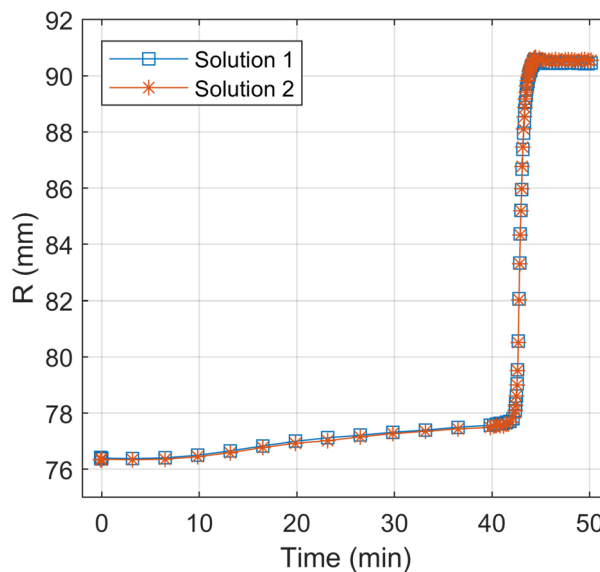


**Fig. 15** Time traces of the radius at  $(X, Z) = (0, 0)$  mm measured from stereo X-ray DIC using either Solution 1 to pre-process the images to recover conservation of intensity or Solution 2 using a specialized path-integrated DIC algorithm

**Table 4** Comparison of benefits and disadvantages of the two proposed solutions to resolve the violation of conservation of intensity of path-integrated X-ray images

	Benefits	Disadvantages
<b>Solution 1, Pre-processing</b>	The code required to pre-process the images is relatively simple and straight forward. Images can be correlated with standard, optical DIC software after pre-processing.	The feature identification algorithm is not easily generalizable to arbitrary patterns and was not wholly robust even for the pattern consisting of distinct circular features used here.
<b>Solution 2, PI-DIC</b>	PI-DIC is a more elegant approach applicable to any pattern, and can be extended to track two or more patterned surfaces moving independently in the X-ray path.	PI-DIC requires a customized, end-to-end implementation of a DIC code, which is significantly more complex than the image pre-processing code for the first solution.

**Table 5** Bounds for the affine subset shape function parameters for PI-DIC, relative to the initializations

Parameter	Bounds
Normal strains, $P_{xx}$ and $P_{yy}$	$\pm 0.60$
Shear strains, $P_{xy}$ and $P_{yx}$	$\pm 0.15$
Displacements, $P_u$ and $P_v$	$\pm 10$ px

To quantify the agreement between the two solutions, results for Solution 1 were interpolated to the point cloud locations of Solution 2 (in the reference configuration), and the root-mean-square (RMS) discrepancy between the two solutions was computed. The RMS discrepancy was computed on point-wise basis for all points in central region of the ROI ( $-40 \leq X \leq 40$  mm and  $-40 \leq Z \leq 40$  mm), for each time step. The RMS discrepancy for the radius is approximately 0.1 mm in the first portion of the test before the unit had deformed significantly (times less than approximately 42.5 min.), and rises to 0.3 mm in the second portion of the test. Given a maximum change in radius on the order of 10–15 mm by the end of the test, discrepancies of less than 0.3 mm indicate agreement between the two solutions within approximately 2–3%.

## Conclusions

A test series was previously conducted in which an aluminum-skinned, fiber-epoxy composite cylinder was subjected to radiant heating mimicking an adjacent fire. The overarching goal was to characterize the safe use of such composites for aviation and aerospace industries in the case of fire accident scenarios, where additional hazards are introduced from epoxy decomposition, pressurization and combustion.

Harsh environmental conditions precluded physical strain gauges or optical DIC for deformation measurements, motivating the use of X-ray DIC. A tantalum DIC pattern was

applied to the test unit, and *in situ* X-ray images from a stereo system were acquired. However, heater rods from the thermal chamber were visible in the X-ray images, violating conservation of intensity for the patterned surface of interest on the test unit and causing optical DIC software to fail.

Two solutions were developed to resolve the violation of conservation of intensity. First, images were pre-processed to isolate the DIC pattern from the path-integrated X-ray images. These corrected images were then correlated with standard, optical DIC software. Second, the matching criterion for DIC was modified to account for multiple, independently-moving components contributing to the final image intensity. This “Path-Integrated DIC” (PI-DIC) algorithm was extended from a 2D framework to a stereo framework and implemented in a custom DIC software.

Both solutions accurately measured the cylindrical shape of the undeformed test unit, recovering radii values of  $R = 76.20 \pm 0.12$  mm compared to the theoretical radius of  $R_{theor} = 76.20$  mm. During the test, the test unit pressurized and bulged asymmetrically toward a jet of burning epoxy decomposition gasses that locally increased the thermal flux. Both solutions measured the heterogeneous change in radius of this bulge, which reached a maximum of approximately  $R = 91$  mm. The RMS discrepancy between the two solutions was 2–3%, lending high confidence to the measurements. Given comparable accuracies, the benefits and disadvantages of the two solutions are summarized in Table 4.

Ultimately, the *in situ* deformation measurements of the test unit afforded through stereo X-ray DIC will be fused with the concurrent temperature and pressure measurements to characterize the thermo-mechanical response of the test unit. This combined experimental data can be used to validate a computational model of the epoxy decomposition, which will aid in safe design of components for aviation and aerospace industries in fire accident scenarios. Additionally, the two solution methods documented here to resolve the violation of conservation of intensity for path-integrated X-ray images can be applied to future experiments for either DIC or PIV in complex or extreme environments.



## Appendix: Initializations of 2D PI-DIC Algorithm

Determining appropriate initializations for DIC in general is non-trivial and the subject of many research papers in the DIC community, e.g. [37–46]. Previous results for PI-DIC specifically showed that the PI-DIC algorithm converges on the correct solution for  $P_{PI}^*$  only if an initialization is seeded within 2 px of the final result [27]. The present work utilized a pragmatic and somewhat manual approach to determine appropriate initializations with the ultimate aim being to incorporate PI-DIC into an established DIC software that already has suitable initialization algorithms. Overall, initializations were only provided for the four displacement parameters ( $P_{u,F_2}$ ,  $P_{v,F_2}$ ,  $P_{u,G_{PI}}$  and  $P_{v,G_{PI}}$ ). The eight warping parameters ( $P_{xx,F_1}$ ,  $P_{xy,F_1}$ ,  $P_{yx,F_1}$ ,  $P_{yy,F_1}$ ,  $P_{xx,F_2}$ ,  $P_{xy,F_2}$ ,  $P_{yx,F_2}$ , and  $P_{yy,F_2}$ ) were initialized at zero for every subset in every image.

### Initializations of the Path-Integrated Images

First, either 15 or 25 seed points, for Cam0 and Cam1, respectively, were manually identified in the full-resolution versions ( $2560 \times 2160$  px<sup>2</sup>) of the synthetic reference image of the DIC pattern,  $F_1$ , and the undeformed, path-integrated image,  $G_{PI}^1$ . Next, a two-dimensional cubic polynomial was fit to the locations of these seed points and evaluated at 50 px intervals to provide a finer grid of seed points. The coordinates of the seed points were then divided by 5 to align with the binned image size ( $512 \times 432$  px<sup>2</sup>).

As the correlation progressed through the time series of images, a bilinear interpolant was created for the displacements of the previous path-integrated image ( $P_{u,G_{PI}}^{j-1}$  and  $P_{v,G_{PI}}^{j-1}$ ). The interpolant was evaluated to provide initializations for displacements of the current path-integrated image ( $P_{u,G_{PI}}^j$  and  $P_{v,G_{PI}}^j$ ). Thus, if a point failed to correlate in one image, an initialization was still provided for that point in future images by interpolating the displacements from neighboring points.

### Initializations of the Pseudo Light-Field Referencelimage

The pseudo light-field reference image of the thermal chamber,  $F_2$ , lacked sufficient intensity gradients to be well tracked on its own. As a result, subsets in this image were frequently poorly identified, with unrealistically large warping parameters ( $P_{xx,F_2}$ ,  $P_{xy,F_2}$ ,  $P_{yx,F_2}$ , and  $P_{yy,F_2}$ ) and large vertical displacements ( $P_{v,F_2}$ ). To correct this behavior, two additional constrictions were placed on the initializations for image  $F_2$ .

First, because the heater rods remained nominally stationary while the test unit deformed, the DIC pattern appeared to deform over a nominally fixed background image. This behavior is illustrated in Fig. 8 in the main text, where both the purple subset of the path-integrated image and the blue subset of the pseudo light-field image started centered over one of the heater rods at time step 1 and translated to the edge of the heater rod in time step  $j$ . Therefore, the initializations for the displacement parameters of the thermal chamber subsets ( $P_{u,F_2}^j$  and  $P_{v,F_2}^j$ ) were set to the same values as the initializations of the displacement parameters of the path-integrated subsets ( $P_{u,G_{PI}}^j$  and  $P_{v,G_{PI}}^j$ ). Second, bounds were placed on the optimization parameters, relative to the initializations, as reported in Table 5.

**Acknowledgements** The test series to characterize the thermo-mechanical response of the aluminum-skinned, fiber-epoxy composite test units was highly collaborative, with innumerable people contributing to the test unit design and fabrication, computational simulation, and test execution. The author is especially thankful to Brent Houchens for his visionary support of X-ray DIC for this test series, Enrico Quintana for his expertise in designing and performing *in situ* X-ray imaging, Ethan Zepper as test director leading the team, Samuel Fayad for contributions to the PI-DIC algorithm and peer review, Caroline Winters for funding support and peer review, and Phillip Reu for DIC expertise and peer review.

**Funding** This article has been authored by an employee of National Technology and Engineering Solutions of Sandia, LLC under Contract No. DE-NA0003525 with the U.S. Department of Energy (DOE). The employee owns all right, title and interest in and to the article and is solely responsible for its contents. The United States Government retains and the publisher, by accepting the article for publication, acknowledges that the United States Government retains a non-exclusive, paid-up, irrevocable, world-wide license to publish or reproduce the published form of this article or allow others to do so, for United States Government purposes. The DOE will provide public access to these results of federally sponsored research in accordance with the DOE Public Access Plan, <https://www.energy.gov/downloads/doe-public-access-plan>. This paper describes objective technical results and analysis. Any subjective views or opinions that might be expressed in the paper do not necessarily represent the views of the U.S. Department of Energy or the United States Government.

**Data Availability Statement** Data sets and raw images generated during the current study are available from the corresponding author on reasonable request.

### Declarations

**Conflict of Interest** The author declares she has no conflict of interest.

### References

- Schreier H, Orteu JJ, Sutton MA (2009) Image correlation for shape, motion and deformation measurements. Springer, US. <https://doi.org/10.1007/978-0-387-78747-3>
- Raffel M, Willert CE, Scarano F, Kähler CJ, Wereley ST, Kompenhans J (2018) Particle image velocimetry, 3rd edn. Springer International Publishing AG. <https://doi.org/10.1007/978-3-319-68852-7>

3. Jones EMC, Reu PL (2017) Distortion of digital image correlation (DIC) displacements and strains from heat waves. *Exp Mech* 58(7):1133–1156. <https://doi.org/10.1007/s11340-017-0354-3>
4. Lynch KP, Jones EMC, Wagner JL (2020) High-precision digital image correlation for investigation of fluid-structure interactions in a shock tube. *Exp Mech* 60(8):1119–1133. <https://doi.org/10.1007/s11340-020-00610-8>
5. Smith CM, Hoehle MS (2018) Imaging through fire using narrow-spectrum illumination. *Fire Technol* 54:1705–1723. <https://doi.org/10.1007/s10694-018-0756-5>
6. Abotula S, Heeder N, Chona R, Shukla A (2013) Dynamic thermo-mechanical response of Hastelloy X to shock wave loading. *Exp Mech* 54(2):279–291. <https://doi.org/10.1007/s11340-013-9796-4>
7. Pan B, Wu D, Wang Z, Xia Y (2011) High-temperature digital image correlation method for full-field deformation measurement at 1200 °C. *Meas Sci Technol* 22(1):1–11. <https://doi.org/10.1088/0957-0233/22/1/015701>
8. Gupta S, Parameswaran V, Sutton MA, Shukla A (2014) Study of dynamic underwater implosion mechanics using digital image correlation. *Proc R Soc A* 470(2172):1–17. <https://doi.org/10.1098/rspa.2014.0576>
9. Reu PL, Miller TJ (2008) The application of high-speed digital image correlation. *J Strain Anal Eng* 43(8):673–688. <https://doi.org/10.1243/03093247jsa414>
10. Pankow M, Justusson B, Waas AM (2010) Three-dimensional digital image correlation technique using single high-speed camera for measuring large out-of-plane displacements at high framing rates. *Appl Opt* 49(17):3418–27. <https://doi.org/10.1364/AO.49.003418>
11. Marimon Giovannetti L, Banks J, Turnock SR, Boyd SW (2017) Uncertainty assessment of coupled digital image correlation and particle image velocimetry for fluid-structure interaction wind tunnel experiments. *J Fluid Struct* 68:125–140. <https://doi.org/10.1016/j.jfluidstructs.2016.09.002>
12. Spottswood SM, Bebernis TJ, Eason TG, Perez RA, Donbar JM, Ehrhardt DA, Riley ZB (2019) Exploring the response of a thin, flexible panel to shock-turbulent boundary-layer interactions. *J Sound Vib* 443:74–89. <https://doi.org/10.1016/j.jsv.2018.11.035>
13. Su Z, Pan J, Zhang S, Wu S, Yu Q, Zhang D (2022) Characterizing dynamic deformation of marine propeller blades with stroboscopic stereo digital image correlation. *Mech Syst Signal Pr* 162. <https://doi.org/10.1016/j.ymsp.2021.108072>
14. Su Z, Pan J, Lu L, Dai M, He X, Zhang D (2021) Refractive three-dimensional reconstruction for underwater stereo digital image correlation. *Opt Express* 29(8):12131–12144. <https://doi.org/10.1364/OE.421708>
15. Ellis CL, Hazell P (2020) Visual methods to assess strain fields in armour materials subjected to dynamic deformation—a review. *Appl Sci* 10(8). <https://doi.org/10.3390/app10082644>
16. Russell SS, Sutton MA (1989) Strain-field analysis acquired through correlation of X-ray radiographs of a fiber-reinforced composite laminate. *Exp Mech* 29(2):237–240. <https://doi.org/10.1007/bf02321382>
17. Synnergren P, Goldrein HT, Proud WG (1999) Application of digital speckle photography to flash X-ray studies of internal deformation fields in impact experiments. *Appl Opt* 38(19):4030–6. <https://doi.org/10.1364/ao.38.004030>
18. Prentice HJ, Proud WG, Walley SM, Field JE (2010) The use of digital speckle radiography to study the ballistic deformation of a polymer bonded sugar (an explosive simulant). *Int J Impact Eng* 37(11):1113–1120. <https://doi.org/10.1016/j.ijimpeng.2010.05.003>
19. Grantham SG, Goldrein HT, Proud WG, Field JE (2016) Digital speckle radiography—a new ballistic measurement technique. *Imaging Sci J* 51(3):175–186. <https://doi.org/10.1080/13682199.2003.11784423>
20. Rae PJ, Williamson DM, Addiss J (2010) A comparison of 3 digital image correlation techniques on necessarily suboptimal random patterns recorded by X-ray. *Exp Mech* 51(4):467–477. <https://doi.org/10.1007/s11340-010-9444-1>
21. Louis L, Wong TF, Baud P (2007) Imaging strain localization by X-ray radiography and digital image correlation: Deformation bands in Rothbach sandstone. *J Struct Geol* 29(1):129–140. <https://doi.org/10.1016/j.jsg.2006.07.015>
22. Bay BK (1995) Texture correlation: A method for the measurement of detailed strain distributions within trabecular bone. *J Orthop Res* 13(2):258–67. <https://doi.org/10.1002/jor.1100130214>
23. Synnergren P, Goldrein HT (1999) Dynamic measurements of internal three-dimensional displacement fields with digital speckle photography and flash X-rays. *Appl Opt* 38(28):5956–61. <https://doi.org/10.1364/ao.38.005956>
24. Jones EMC, Quintana EC, Reu PL, Wagner JL (2019) X-ray stereo digital image correlation. *Exp Tech* 44(2):159–174. <https://doi.org/10.1007/s40799-019-00339-7>
25. James JW, Jones EMC, Quintana EC, Lynch KP, Halls BR, Wagner JL (2021) High-speed X-ray stereo digital image correlation in a shock tube. *Exp Tech* 46(6):1061–1068. <https://doi.org/10.1007/s40799-021-00508-7>
26. Rohe DP, Quintana EC, Witt BL, Halls BR (2020) Structural dynamic measurements using high-speed X-ray digital image correlation. IMAC XXXIX, Virtual Conference, SAND2020-13702C
27. Jones EMC, Fayad SS, Quintana EC, Halls BR, Winters C (2023) Path-integrated X-ray images for multi-surface digital image correlation (PI-DIC). *Exp Mech*. <https://doi.org/10.1007/s11340-023-00949-8>
28. Parker JT, Deberardinis J, Mäkiharju SA (2022) Enhanced laboratory X-ray particle tracking velocimetry with newly developed tungsten-coated O(50 µm) tracers. *Exp Fluids* 63(12). <https://doi.org/10.1007/s00348-022-03530-6>
29. Parker JT, Mäkiharju SA (2022) Experimentally validated X-ray image simulations of 50 µm X-ray PIV tracer particles. *Meas Sci Technol* 33(5). <https://doi.org/10.1088/1361-6501/ac4c0d>
30. Antoine E, Buchanan C, Fezzaa K, Lee WK, Rylander MN, Vlachos P (2013) Flow measurements in a blood-perfused collagen vessel using X-ray micro-particle image velocimetry. *PLoS One* 8(11):e81198. <https://doi.org/10.1371/journal.pone.0081198>
31. Park H, Yeom E, Lee SJ (2016) X-ray PIV measurement of blood flow in deep vessels of a rat: An in vivo feasibility study. *Sci Rep* 6(1):19194. <https://doi.org/10.1038/srep19194>
32. Jones EMC, Quintana EC, Zepper ET, Murphy AW, Houchens BC (2023) Characterizing thermal-mechanical response of materials in fire environments with combined stereo X-ray digital image correlation, traditional instrumentation, and simulations. In preparation
33. Murphy AW, Zepper ET, Jones EMC, Quintana EC, Montoya MM, Cruz-Cabrera AA, Scott SN, Houchens BC (2021) Response of aluminum-skinned carbon-fiber-epoxy to heating by an adjacent fire. 12th U.S. National Combustion Meeting, Organized by the Central States Section of the Combustion Institute, College Station, TX
34. International Digital Image Correlation Society (iDICs), Jones EMC, Iadicola MA (2018) A good practices guide for digital image correlation, 1st edn. <https://doi.org/10.32720/idics/gpg.ed1>
35. Fayad SS, Jones EMC, Winters C (2023) Path-integrated X-ray digital image correlation with synthetic reference images. Submitted to *Exp Tech*
36. Pan B, Xie H, Wang Z (2010) Equivalence of digital image correlation criteria for pattern matching. *Appl Opt* 49(28):5501–9. <https://doi.org/10.1364/AO.49.005501>
37. Wang Z, Vo M, Kieu H, Pan T (2014) Automated fast initial guess in digital image correlation. *Strain* 50(1):28–36. <https://doi.org/10.1111/str.12063>
38. Zhang J, Lu H, Baroud G (2018) An accelerated and accurate process for the initial guess calculation in digital image correlation algorithm. *AIMS Mat Sci* 5(6):123–1241. <https://doi.org/10.3934/matersci.2018.6.1223>

39. Simončič S, Klobčar D, Podržaj P (2015) Kalman filter based initial guess estimation for digital image correlation. *Opt Laser Eng* 73:80–88. <https://doi.org/10.1016/j.optlaseng.2015.03.001>
40. Pan B, Wang Y, Tian L (2017) Automated initial guess in digital image correlation aided by Fourier-Mellin transform. *Opt Eng* 56(1):014103. <https://doi.org/10.1117/1.OE.56.1.014103>
41. Zhang Y, Yan L, Liou F (2018) Improved initial guess with semi-subpixel level accuracy in digital image correlation by feature-based method. *Opt Laser Eng* 104:149–158. <https://doi.org/10.1016/j.optlaseng.2017.05.014>
42. Li W, Li Y, Liang J (2019) Enhanced feature-based path-independent initial value estimation for robust point-wise digital image correlation. *Opt Laser Eng* 121:189–202. <https://doi.org/10.1016/j.optlaseng.2019.04.016>
43. Wang L, Bi S, Li H, Gu Y, Zhai C (2020) Fast initial value estimation in digital image correlation for large rotation measurement. *Opt Laser Eng* 127:105838. <https://doi.org/10.1016/j.optlaseng.2019.105838>
44. Zou X, Pan B (2021) Full-automatic seed point selection and initialization for digital image correlation robust to large rotation and deformation. *Opt Laser Eng* 138:106432. <https://doi.org/10.1016/j.optlaseng.2020.106432>
45. Yang H, Wang S, Xia H, Liu J, Wang A, Yang Y (2022) A prediction-correction method for fast and accurate initial displacement field estimation in digital image correlation. *Meas Sci Technol* 33(10):105201. <https://doi.org/10.1088/1361-6501/ac7a06>
46. Ma X, Ren Q, Zhao D, Zhao J (2022) Convolutional neural network based displacement gradients estimation for a full-parameter initial value guess of digital image correlation. *Opt Continuum* 1(10):2195–2211. <https://doi.org/10.1364/optcon.471914>

**Publisher's Note** Springer Nature remains neutral with regard to jurisdictional claims in published maps and institutional affiliations.

Springer Nature or its licensor (e.g. a society or other partner) holds exclusive rights to this article under a publishing agreement with the author(s) or other rightsholder(s); author self-archiving of the accepted manuscript version of this article is solely governed by the terms of such publishing agreement and applicable law.